Shared ligand-blocking mechanism but distinct conformational modulation by α5-targeting antibodies BIIG2 and MINT1526A

Adam Nguyen[1,2], Joel B. Heim[3,4,6], Gabriele Cordara[4], Matthew C. Chan[1], Hedda Johannesen[4], Cristine Charlesworth[5], Ming Li[3], Caleigh M. Azumaya[1,7], Benjamin Madden[5], Ute Krengel[4], Alexander Meves[3*] and Melody G. Campbell[1,2*]

1. Basic Sciences Division, Fred Hutchinson Cancer Center, Seattle, Washington 98109, USA
2. Biological Physics Structure and Design Program, University of Washington, Seattle, Washington 98195, USA
3. Department of Dermatology, Mayo Clinic, Rochester, Minnesota 55905, USA
4. Department of Chemistry, University of Oslo, NO-0315 Oslo, Norway
5. Medical Genome Facility, Proteomics Core, Mayo Clinic, Rochester, Minnesota 55905, USA
6. Current Address: Nykode Therapeutics, Oslo Science Park, 0349 Oslo, Norway
7. Current Address: Genentech, South San Francisco, California 94080, USA

*Corresponding Authors
Alexander Meves. E-mail: meves.alexander@mayo.edu
Melody G. Campbell. E-mail: melody@fredhutch.org

Abstract:

Integrins are heterodimeric receptors important for cell adhesion and signaling. Integrin α5β1 is a key mediator of angiogenesis and its dysregulation is associated with tumor progression and metastasis. Despite numerous efforts, α5β1-targeting therapeutics have been unsuccessful due to poor efficacy and off-target effects. A contributing factor is our limited understanding of how integrin conformation influences interactions with therapeutics. Using cell-based functional assays, patient derived xenografts, biophysics, and electron microscopy, we shed light on these relationships by characterizing two anti-α5β1 antibodies, BIIG2 and MINT1526A. We show that both antibodies bind α5β1 with nanomolar affinity, reduce angiogenesis *in vitro*, and bind overlapping epitopes that block fibronectin binding. However, using cryoEM, we reveal that while BIIG2 binding doesn't alter the conformational states, MINT1526A restricts α5β1's range of flexibility. These insights can guide which aspects to prioritize and improve the design of future integrin-targeted therapeutics.

Introduction

Integrin heterodimers, which consist of an α subunit and a β subunit, are type-I transmembrane receptors that play vital roles in immune response, cell motility, cell-matrix interactions, signaling, proliferation, and apoptosis **(Supplemental Figure. S1A;** [1]). Pathologies linked to integrins include autoimmune, cardiac, pulmonary, neurodegenerative, hematologic, and oncologic conditions [2]. Integrins have long been identified as promising therapeutic targets. Although numerous integrin-targeting therapeutics have entered clinical trials, fewer than a dozen have been approved and marketed, while others have been withdrawn due to limited efficacy and adverse effects [3,4].

Integrin α5β1 plays a key role in facilitating cell migration during angiogenesis and is one of several integrins that recognize the conserved arginine-glycine-aspartate (RGD) sequence motif found in several extracellular matrix (ECM) proteins. The primary α5β1 ligand, fibronectin (FN), is a glycoprotein that scaffolds other matrix proteins and cells. α5β1 participates in tumor angiogenesis, among other pathologically significant processes related to human diseases [5–7]. Like many other well-studied integrins, α5β1 adopts three conformations which can be directly linked to α5β1 activation: bent, extended closed, and extended open **(Supplemental Figure. S1B)**. The extended open conformation is stabilized by FN via two interactions: the canonical integrin binding RGD motif and an additional synergy site. Specifically, a fibronectin domain (type III domain 10, FN10) contains an RGD motif that inserts into the α and β subunit interface [8,9] and a second domain, FN9 contains the synergy site that facilitates a catch-bond interaction with the β-propeller of the α5 subunit [9–13].

The increased expression of integrins α5β1, αvβ3, and αvβ5 in new blood vessels during the angiogenic switch in tumors underscores their significance as potential targets for therapeutic intervention [14,15]. Early-phase clinical trials involving patients with advanced solid tumors investigated multiple monoclonal antibodies targeting α5β1 function, however, these trials did not demonstrate clear efficacy. [16–18]. Among the tested antibodies was MINT1526A (RG-7594), a fully humanized IgG1 antibody specifically formulated to block α5β1 function [18]. A different α5β1 inhibiting antibody, BIIG2, was developed to inhibit human JAR choriocarcinoma cells binding to ECM proteins by immunization of Lewis rats [19]. Follow-up studies showed that BIIG2 was effective in both inhibiting fibronectin attachment and identifying invasive cytotrophoblasts within the human placenta [19,20]. We evaluated BIIG2 and MINT1526A using structural, biophysical, and cell-based methods to define the mechanisms underlying antibody-mediated α5β1 inhibition. We found that BIIG2 shows more favorable inhibitory outcomes *in vitro* when compared to MINT1526A, and the two antibodies elicit different effects on conformations accessible to α5β1. Since integrin conformation has been shown to influence the severity of off-target effects [3,4], our results provide the molecular basis for the design of future integrin-targeted therapeutics.

Results

BIIG2 and MINT1526A antibodies reduce angiogenesis in vitro; BIIG2 to a greater extent

We employed both two and three-dimensional angiogenesis assays to evaluate how BIIG2 and MINT1526A influence angiogenesis. First, we used a spheroid-based cellular angiogenesis assay with human umbilical vein endothelial cells (HUVEC) to measure cumulate sprouting length as a proxy to angiogenic potential by induction with vascular endothelial growth factor (VEGF). Sunitinib, a tyrosine kinase inhibitor known to inhibit angiogenesis [21], was used as a positive control and reduced VEGF-induced HUVEC sprouting with an IC_{50} of 69 nM (**Figure 1A)**. Treatment with BIIG2 showed comparable inhibitory effect with an IC_{50} of 50 nM. The concentration series of MINT1526A used was insufficient to derive an IC_{50} value, however, these spheroids, when treated with MINT1526A did not have the same level of sprouting as VEGF-induced, suggesting a minor effect on angiogenic potential. Negative control of human and rat IgG showed no impact on sprouting (IC_{50} > 1000 nM). To support these findings, we performed a two-dimensional tube formation assay by cultivating HUVEC on Matrigel and inducing tube formation with VEGF (**Figures 1B**). At 10 nM and 100 nM, BIIG2 inhibits VEGF mediated angiogenesis more potently than MINT1526A as defined by the reduction of total master segment lengths (length of vessel between junctions) and the number of meshes or junctions. BIIG2 exhibits a dose dependent manner trend in the reduction of both segment lengths and number of meshes. In both two- and three-dimensional assays, BIIG2 displays a greater reduction of VEGF-induced growth of HUVEC and is more effective than MINT15262A *in vitro*.

BIIG2 localizes to connective tissue-resident fibroblasts and melanoma cells

Integrin α5β1 is expressed on various tissues at low levels [22]. We used immunohistochemistry to determine the cellular localization and tissue specificity of BIIG2 and compared the polyclonal α5 integrin antibody PA5-82027. As expected, PA5-82027 stains a broad spectrum of human tissues, including placental syncytiotrophoblasts, striated ducts in salivary glands, and alveolar ducts **(Supplemental Figure S2A and Table S3)**. In contrast, BIIG2 exhibits a restricted staining profile, predominantly marking isolated connective tissue-resident fibroblasts across various tissues. Remarkably, BIIG2 also demonstrated intense staining of activated and transformed melanocytes in the epidermis and upper dermis derived from patients with atypical nevi and invasive cutaneous melanoma **(Supplemental Figure S2B)**. Tissue specificity in therapeutics is advantageous since it has the potential to reduce off-target effects and BIIG2's specificity supports the targeted treatment of various pathologies, including fibrosis, sclerosis, and melanoma.

BIIG2 reduces tumor volume in patient-derived xenograft models

Based on the strong BIIG2 immunohistochemical staining localized to human melanoma cells (**Supplemental Figure S2B**), and considering the known tumor-inhibitory effects of other anti-α5

antibodies in rhabdomyosarcoma and glioblastoma mouse models [23,24], we established two melanoma xenograft cultures to evaluate the *in vivo* inhibitory effects of BIIG2 on melanoma growth. Using brain metastases from patients who had different responses to treatment (**Supplemental Figure S3A-C**), we derived two cultures, M15 and M12. The *NRAS*^{Q61}-mutant M15 cells demonstrated metastasis and resistance to radiation and systemic therapy, while the *BRAF*^{V600}-mutant M12 cells responded well to systemic therapy, and the patient achieved complete remission [25]. Quantitative PCR of M15 and M12 shows differing levels of melanoma markers compared to normal human melanocytes (NMH) such as melan-A (*MLANA)* and microphthalmia-associated transcription factor (*MITF)*, *CDKN2A* tumor suppressor, and higher mRNA expression of α5 integrin ligands *FN1 (fibronectin)*, tenascin C (*TNC)*, and osteopontin (*SPP1)* compared to M12 **(Supplemental Figure S3D)**. Furthermore, cell surface integrin flow cytometry showed that compared to NHM, αv and α5 are upregulated in M15 and M12 cells, with the highest α5 expression in M15 cells **(Supplemental Figure S3E)**. Increased α5 expression in human melanoma tissue is in agreement with previous reports [14,26].

M15 and M12 cells were embedded in Matrigel to grow and subsequently injected into the flanks of athymic mice to determine its effectiveness on tumor volumes *in vivo* (**Figure 2A**). When tumors became palpable, antibodies were administered intraperitoneally at a dosage of 10 mg/kg twice weekly. Treatments were stopped when the tumors injected with control IgG surpassed an average volume of 1000 mm^3. BIIG2 slowed, but did not completely inhibit tumor growth in both the M15 and the M12 model (**Figure 2B**). We found that BIIG2 reduced tumor volume of both M12 and M15 models (T-test = 0.01 and 0.04 respectively). BIIG2 displayed greater and more consistent tumor growth inhibition than other integrin-targeting antibodies, including P1F6, P3G8, P5H9 (anti-αv), and P1D6 (anti-α5) [23,24] within the M12 xenograft model (**Figure 2B**). However, within M15, there is no statistically significant difference in effectiveness between BIIG2 and the other antibodies. Expression analysis revealed that in BIIG2-treated mice, the xenografted M12 tumors exhibited an increase in RNA levels of *MLANA* and *p53* by 50% and 32% respectively, in comparison to those treated with control IgG (n = 9 mice per group; T-test $p < 0.01$; Data not shown). Pentamidine isethionate (Pentam), has been observed to restore p53 levels in melanoma cells [27]. BIIG2 has similar efficacy compared to pentamidine in both M12 and M15 xenograft models. Combinatory treatments can be a method to increase treatment efficacy, however a combination treatment of BIIG2 and Pentam, tumor volume was further reduced but not by a significant amount. (**Figure 2C**). The clinically validated MINT1526A could not be used for comparison due to a shortage of purified antibody, which was kindly provided by Genentech.

BIIG2 and MINT1526A bind α5β1 with sub-nanomolar affinity independent of integrin activation state

Having established the potential of BIIG2 in angiogenesis and melanoma tumor growth inhibition, we characterized the affinities of BIIG2 and MINT1526A to α5β1, a critical consideration for effective therapeutics. Integrin function, signaling, and its ability to bind ligands are linked to its conformation and can be influenced *in vitro* using divalent cations [1]. In β1 integrins, calcium (Ca^{2+}) is known to promote a

bent conformation which is linked to inactive integrins, while manganese (Mn^{2+}) favors an open conformation, which is linked to integrin activity [28,29]. We used biolayer interferometry (BLI) to determine the binding affinities of BIIG2 and MINT1526A to recombinant human α5β1 ectodomain in the presence of 5 mM Ca^{2+} or 1 mM Mn^{2+}. We found that both antibodies bind integrin in the low nanomolar range irrespective of the presence of Ca^{2+} or Mn^{2+}: BIIG2 binds to α5β1 with an affinity of 0.57 nM in Ca^{2+} and 0.64 nM in Mn^{2+}; MINT1526A binds α5β1 with an affinity of 1.3 nM in Ca^{2+} and 0.23 nM in Mn^{2+}. In regards to antibody affinities, all values are relatively close and considered high-affinity (**Figure 3A**). These findings suggest that the activation state and in turn, the conformation of α5β1 does not greatly influence the affinity of either antibody.

We hypothesized that the antibody-mediated reduction in angiogenesis is due to steric inhibition of α5β1 binding to fibronectin. Therefore, we conducted a series of competition experiments using BLI to determine if BIIG2 and MINT1526A prevent α5β1 from binding to fibronectin, using a recombinant truncated fibronectin fragment (FN7-10) that contains the necessary domains for α5β1 binding [9,12]. Consistent with prior studies, we show that α5β1 binds FN7-10 with a high affinity in the presence of Mn^{2+}, whereas in high Ca^{2+}, α5β1 shows significantly reduced affinity to FN7-10 [9,28]. In the presence of Mn^{2+}, we find that if α5β1 is pre-incubated with either BIIG2 or MINT1526A, there is a marked decrease in FN7-10 binding (**Supplemental Figure S4**). Likewise, when pre-incubating integrin with FN7-10, neither antibody was able to bind, suggesting that the fibronectin, BIIG2 and MINT1526A share a similar or overlapping binding interface as they are unable to displace each other once bound to α5β1. As anticipated α5β1 does not bind FN7-10 with high affinity in high Ca^{2+} conditions. We find that in the same cation conditions, that BIIG2 and MINT1526A bind integrin at only a slightly lower affinity than if FN7-10 is not present.

MINT1526A restricts the conformations accessible to α5β1; BIIG2 does not

To visualize epitopes and impact of antibody binding on α5β1's conformation, we used single-particle negative stain electron microscopy (nsEM) to visualize the protein complexes of α5β1 ectodomains and purified BIIG2 or MINT1526A Fabs. We generated 2D class averages that consolidate thousands of individual particle images (**Supplemental Figure S5**). As previously hypothesized [18,19], our nsEM analysis confirmed that both BIIG2 and MINT1526A bind the α5 subunit, and we further localized the epitope to the α5 β-propeller domain (**Supplemental Figure S1A**). When looking at α5β1 by itself in inactivating conditions (5 mM Ca^{2+}), most (98%) adopts two conformations: 'bent' and 'extended closed' **(Supplemental Figure S5)**, consistent with previous work [28]. In activating conditions (1 mM Mn^{2+}), we observed an increase in the proportion of α5β1 particles adopting the 'extended open' conformation (24% vs 2%) (**Supplemental Figure S5**). When α5β1 is bound to the BIIG2 Fab, the ratios of integrins in the three different conformations are similar to what we found for apo α5β1 in both activation conditions. (**Figure 3A and Supplemental Figure S5**). In contrast, when MINT1526A binds, the conformational flexibility of α5β1 is drastically restricted, and only the bent conformation was observed in both activating and inactivating conditions (**Supplemental Figure S5**). This suggests that although both antibodies inhibit

α5β1 function by blocking fibronectin binding through steric hindrance, MINT1526A has an additional allosteric effect, altering the global conformational equilibrium and preventing integrin extension and headpiece opening.

High-resolution structural analysis of the BIIG2 Fab reveals occlusion of the integrin binding cleft

We determined the structure of the BIIG2 Fab to 1.4 Å resolution using X-ray crystallography (PDB ID: 8R38; **Figure 4F and Supplemental Figure S6)**. The structure was refined to R/R_{free} values of 19.9/22.4% with good geometry **(Supplemental Table S1**), and is characterized by well-defined electron density from residues 1-210 and 1-214 (Kabat numbering scheme) in the heavy and light chains, respectively. In particular, the antigen-binding site is well-defined. The binding site of the BIIG2 light chain is dominated by positive charges from three lysine residues (K27, K31, and K92) and R28, whereas the heavy chain CDRs are charge-balanced. The BIIG2 CDR H3 loop is exposed, notably longer than the other CDRs and partially involved in crystal contacts through residues T97, M98, G99, and CDR L1 loop R27. The obtained high resolution allowed for accurate modeling of several modified residues. These include a pyroglutamate on the N-terminal position of the heavy chain, a methyllysine on the light chain (L199), and a 5-hydroxyproline modification in the CDR H3 loop (Pro 100C). In addition, we observed well-defined electron density for the only visible glycosylation on BIIG2, located on glycan N60 of the Fv heavy chain.

To map how BIIG2 binds to and inhibits α5β1 function, we used single-particle cryogenic electron microscopy (cryoEM) to determine the structure of the α5β1:BIIG2 Fab complex to a global resolution of 2.7 Å **(Figure 4A and Supplemental Table S2**). After focused refinement, the α5β1 headpiece and the variable region of the BIIG2 Fab interface was estimated at 2.5 Å resolution, which allows for atomic modeling **(Figures 4B and 4C, Supplemental Figures S7)**. The crystal structure of the BIIG2 Fab (PDB ID: 8R38; this work) and the close α5β1 closed headpiece structure (PDB ID: 3VI3; [30]) were docked (rigid body fitting) into our cryoEM density as starting coordinates for model building. From here, we built the α5 β-propeller, the β1 β-I domain and a portion of the hybrid domain, and the variable region of the BIIG2 Fab. As with many cryoEM maps of integrins [9,31–36], our map is anisotropic, with the resolution tapering off away from the well-resolved headpiece. Secondary structural elements for the α5 thigh and β1 hybrid domains are visible, but the resolution is insufficient for residue-level modeling. Additional 3D classification reveals populations of BIIG2-bound integrin in the bent (25%) and extended closed conformations (18%). We note that a significant number of particles (57%) contribute to classes that do not have a strong density for the lower leg region (**Supplemental Figure S10).** We hypothesize that the lower legs could be averaged out due to significant conformational variability or interactions with the air-water interface that compromise the particle integrity and note that all domains are visible in nsEM averages and the molecular weight estimate from size exclusion chromatography (SEC) is consistent with a full α5β1 ectodomain **(Supplemental Figures S5 and S7)**.

Our cryoEM map reveals that BIIG2 engages both the α5 and β1 integrin subunits through electrostatic interactions, with positively charged residues on BIIG2 and key negatively charged residues on the integrin. Two lysine residues on the BIIG2 light chain (K27 and K92) form salt bridges with the known negatively charged α5 synergy site residues E81 and E124 **(Figure 4D)**. The portion of the epitope on the α5 β-propeller is further stabilized by surrounding hydrogen bonds. BIIG2 engages several residues that are necessary for efficient FN binding: D154, a key residue stabilizing the interaction between α5 and the FN9 synergy site, interacts with T100A of the BIIG2 heavy chain, thus occluding FN9 access to this residue **(Figure 4E)** [9,30]. Additionally, R71 of the BIIG2 heavy chain forms a salt bridge with E190 of the specificity-determining loop-2 (SDL-2) of the β1 subunit, providing additional stabilizing interactions in the α5β1:BIIG2 complex **(Figure 4E)**. To further support these observations, we employed all-atom molecular dynamics (MD) simulations of the α5β1 headpiece complex with the BIIG2 Fab. Two microsecond-long trajectories show that the network of hydrogen bonding and electrostatic interactions observed in the cryoEM structure are dynamically involved in maintaining the α5β1:BIIG2 interface **(Figure 4G).**

Unlike fibronectin, BIIG2 does not contain an RGD motif nor does it bind any RGD interacting residues on α5β1. However, in addition to the hydrogen bond network, BIIG2's CDR H3 methionine residues M98 and M100 exhibit long-range sulfur-aromatic interactions with α5 W157 and F155 respectively, further stabilizing the binding interface **(Supplemental Figure S11)** [37]. These interactions, summarized in **Supplemental Table S4**, position BIIG2 to sterically occlude fibronectin from accessing the primary RGD binding site and α5's synergy binding site for FN9.

MINT1526A exclusively binds the α5 subunit and prevents fibronectin binding by blocking the synergy binding site

To directly compare the binding interfaces with the BIIG2 complex, we next determined the cryoEM structure of the MINT1526A Fab bound to the α5β1 ectodomain to a global resolution of 3.1 Å **(Figure 5A and Supplemental Table S2)**. Similar to the α5β1:BIIG2 Fab cryoEM map, the resolution of α5β1:MINT1526A Fab was anisotropic, with the highest-resolution regions (2.8 Å) in the headpiece and at the epitope/paratope interface **(Figure 5A and C and Supplemental Figures S8)**. 3D classification reveals the integrin angle of rotation about the knee region ranges from 90 to 73 degrees, in agreement with previous data **(Supplemental Figure S10)** [9]. MINT1526A exclusively binds the α5 subunit and it does not block the canonical RGD binding site cleft. Although MINT1526A also does not directly interact with any residues on α5β1 required to mediate the FN binding, its epitope overlaps with one of the known FN binding sites, preventing interactions between α5 and the FN9 synergy site **(Figure 5A)**. α5's would-be D154 electrostatic and Y208 proline-aromatic interaction with FN are sterically blocked by the CRD H3 of MINT1526A **(Figure 5E)**. The high affinity of α5β1:MINT1526A is likely achieved primarily by hydrogen bonds, involving residues throughout the epitope **(Figures 5E and 5F)**. MD simulations of

α5β1:MINT1526A Fab indicate that these hydrogen bonding interactions between MINT1526A and α5β1 are stable **(Figure 5D)**. A summary of the interactions can be found in **(Supplemental Table S5).**

Discussion

Integrins play an essential role in cell proliferation, adhesion, migration, and survival, and their dysregulation is attributed to the progression of numerous human diseases including cancer [2]. Due to its important role in tumor angiogenesis, α5β1 has long been identified as a target for cancer therapies [38]. More recently, antibodies targeting α5 integrin have been demonstrated to inhibit the progression of the neurodegenerative disorder amyotrophic lateral sclerosis (ALS) and idiopathic pulmonary fibrosis (IPF), underlining and expanding α5β1's potential as a therapeutic target [39,40]. Understanding the precise molecular interactions mediating integrin-therapeutic interactions will be key for the development of tailored, specific, and effective therapeutics, however, the molecular details of α5β1 with any function-modulating antibody have so far been lacking.

We present a comprehensive functional, structural, and mechanistic characterization of BIIG2, a rat IgG antibody targeting human α5 integrin, demonstrating its potential as a therapeutic candidate. BIIG2 exhibits high affinity for α5β1 and shows intense, tissue-specific binding to connective fibroblasts and melanocytes in melanoma patient tissues, which are known to express elevated levels of active α5β1 integrin. This staining pattern may result from BIIG2's ability to recognize the full spectrum of α5β1 headpiece conformations. BIIG2 more effectively inhibits angiogenesis in both 2D- and 3D- assays compared to MINT1526 (RG-7594), an anti-α5β1 antibody that has already been tested in clinical trials. Using single-particle cryoEM and BLI, we show that both BIIG2 and MINT1526A impede α5β1 activation by sterically blocking fibronectin binding, albeit through different epitopes. In two patient-derived xenograft mouse models, BIIG2 demonstrates superior tumor growth inhibition relative to other anti-integrin antibodies, with efficacy comparable to p53 restoration via pentamidine. Given that BIIG2 is a rat monoclonal antibody, future efforts to humanize it could further enhance its therapeutic applicability and reduce potential immune responses in patients. These findings highlight BIIG2's promise as a potent therapeutic candidate targeting α5β1 integrin.

The dramatic difference in the available conformational states of BIIG2-bound α5β1 vs MINT1526A-bound α5β1 was unexpected, since neither Fab interacts with residues that are known to participate in integrin extension or headpiece opening. The root-mean-square difference of the α5β1 headpiece region in these two models is 0.5 Å, indicating that there are no significant global structural differences when BIIG2 or MINT1526A is bound. The most notable difference in our two integrin models is a loop (residues 27-33) between two β-sheets in the first blade of the α subunit's β-propeller. It is tempting to speculate that like other flexible loops in the α subunit [41], this positioning could be related to the overall conformation of α5β1, since in the MINT-bound bent α5β1 the loop is in a downward pointing position, similar to the recent cryoEM structure of α5β1 in a bent conformation (PDB ID: 7NXD; [9]),

whereas the BIIG2-bound α5β1 has the loop pointing upward, similar to an extended structure from the same study bound to fibronectin (PDB ID: 7NWL). Most published structures of this loop are more similar to the 'up' position of the loop, however, since many of these structures are truncated integrin fragments that do not include the lower leg domains, we cannot be certain if this loop is related to overall conformation [30,42]. Therefore, the underlying cause of the observed differences in α5β1 conformations is not entirely clear although allosteric changes must either be transmitted or recognized by MINT1526A. *In vitro* and *in vivo*, it is assumed that most integrin ectodomains exist in conformational equilibriums [28,43]. Consequently, from our structural and biophysical experiments, we cannot definitively determine whether MINT1526A binds all α5β1 conformations and subsequently 'locks' the integrin into the bent conformation, or if it exclusively binds the bent conformation.

Although integrins have long been identified as promising therapeutic targets, with over 130 clinical trials investigating integrin-targeting therapies, fewer than a dozen therapeutics– either antibodies or small molecules– have reached the market [44]. Several cancer-related integrin therapeutics have progressed to late-stage clinical trials although none have been approved to date [45]. Volociximab, the only candidate targeting α5β1, was well tolerated in phase 1 trials [46], but demonstrated limited efficacy in phase 2 across multiple cancer types [16,47] leading to discontinuation of further development. Many other investigational integrin-targeting therapies in oncology have also been halted due to limited efficacy or safety concerns. Nevertheless, integrins remain validated therapeutic targets, with several approved agents demonstrating significant success in non-oncologic indications [4]. Interest in the field remains strong, with numerous ongoing trials showing promising early results.

One theory posits that the success or failure of some integrin therapeutics depends on selectively targeting specific integrin conformations. This concept is exemplified by Nimotuzumab, an anti-tumor antibody targeting the epidermal growth factor receptor (EGFR). Nimotuzumab permits EGFR to adopt its active conformation and exhibits fewer side effects than other anti-EGFR antibodies, such as Cetuximab, which bind similar epitopes but do not allow the active receptor conformation [48]. For integrins, the selectivity of therapeutics for specific conformations or their influence on integrin conformation, and how those differences translate into tissue specificity, off-target effects, or toxicity remains incompletely characterized, although recent work has begun to shed light on these mechanisms [36,49–51]. Structural and biochemical data are available for several late-stage and marketed therapeutics, including high-resolution structures for five of the seven approved integrin therapeutics. However, since some structures are isolated domains or structures of integrin fragments, or conformation is measured more indirectly using size exclusion chromatography (SEC), the conformational landscape available to the therapeutic-bound integrins remains incomplete [4].

Recently, it has been proposed that partial agonism – linked to stabilizing the open conformation – could be responsible for chronic indications of certain failed integrin therapeutics. A comprehensive study of αIIbβ3 small molecule inhibitors showed that of the inhibitors tested, stabilizing the bent

conformation has led to better therapeutic outcomes than those that stabilize an open conformation. That study also identified a general chemical principle for the design of bent-stabilizing inhibitors and, excitingly, extended the work to show the principle held true for the distantly related integrin α4β1 [49].

On the other hand, studies show that small molecule and antibody inhibitors that stabilize the bent-closed conformation of αvβ6 are not able to lower expression of fibrotic-associated genes in lung epithelial cells as effectively as inhibitors that stabilize the extended-open conformation [52]. Clinical advancement of two potential therapeutics that stabilized the closed avβ6 conformation, antibody BG00011 (the humanized version of 3G9) and the small molecule MORF-720 were halted due to suspected on-target safety signals [40,53,54]. In contrast, PLN-74809, which binds all conformations of avβ6 and avβ1 [55] and GSK3008348, which causes rapid internalization of avβ6 [56] which is associated with an active conformation, have led to more promising initial results with no serious adverse effects related to the compounds in clinical trials [57,58]. Similarly, Etaracizumab, an enhanced form of Vitaxin, is well-tolerated in patients [59] and currently under investigation for cancers [60]. Its precursor, LM609 has been shown to bind all conformations of integrin αvβ3 [61].

It has become clear that the challenges associated with integrin-therapeutic development remain numerous, however, exciting recent results linking functional and known clinical outcomes to structural interactions have enabled recent leaps in the establishing of principles that govern effective therapeutics [49]. Significant efforts have advanced the discovery of novel integrin therapeutics including a new platform for antibody discovery [62] and the development of *de novo* structure-based rational-designed integrin miniproteins [36]. In addition to the specific structural and functional details of α5β1-antibody interactions, the results presented here contribute to the greater understanding of the complex interplay between potential integrin therapeutics, conformation, and down-stream effects.

Resource Availability

All structures and models referenced have been deposited in the EMDB and the PDB. The accession numbers for maps and models are as follows: the α5β1:BIIG2 complex EMD-44386 and PDB ID 9B9J; the BIIG2 fab crystal structure: PDB ID 8R38; the α5β1:MINT1526A complex EMD-44387 and PDB ID 9B9K. Two cryoEM data sets have been deposited in the EMPIAR database, each containing raw movies, aligned micrographs and stacks. The accession numbers are as follows: α5β1:BIIG2 (EMPIAR-12552); α5β1:MINT1526A (EMPIAR-12553). Analysis scripts for molecular dynamics simulations are available at https://github.com/CampbellLab2020/nguyen_2023. Simulation trajectories and topology files are available on Zenodo at https://doi.org/10.5281/zenodo.10070033.

Lead Contact

Further information and requests for resources and reagents should be directed to and will be fulfilled by the lead contacts, Alexander Meves (meves.alexander@mayo.edu) and Melody G. Campbell (melody@fredhutch.org).

Author Contributions

AN, JBH, AM and MGC designed the research. CC and ML expressed and purified BIIG2 antibody and prepared BIIG2 and MINT1526A Fab fragments. CC and BM prepared, performed and analyzed mass spectrometry data. AN analyzed the spheroid and tube formation assays. AN, JBH and AM analyzed the tumor xenograft data. JBH performed and analyzed the quantitative PCR experiments. JBH and AM performed and analyzed the immunohistochemistry data. JBH, GC, HJ and UK prepared, collected and analyzed x-ray crystallography data. AN designed, cloned, expressed and purified recombinant α5β1 for experimentation. AN performed and analyzed BLI assays. AN prepared samples, collected and processed negative stain EM data. AN, CMA and MGC prepared samples and collected cryoEM data. AN and MGC processed the cryoEM data. AN built the cryoEM models. MCC designed, performed and analyzed the molecular dynamics simulations. AN, JBH, AM and MGC wrote the initial manuscript. All authors contributed to the edition and discussion of the manuscript.

Acknowledgements

Funding for this research was supported by the National Institutes of Health under Grant K08 CA215105 (A.M.) and R35 GM147414 (M.G.C.). Additional support to M.G.C. was provided by the Seattle Cancer Consortium Safeway Pilot Awards (funded through the NIH/NCI Cancer Center Support Grant P30 CA015704), the Pew Biomedical Scholars award, and Mike and Debbie Koss. A.N. is supported by NHLBI F31 Fellowship 1F31HL174166. MCC was supported by the Interdisciplinary Training Grant in Cancer Research Program (NCI T32 CA080416) through Fred Hutchinson Cancer Center and the Mahan Fellowship; this fellowship is made possible by funding from Mark and Nikki Mahan. J.B.H. was supported

by a Mayo Clinic Smith Gibson Research Fellowship award, J.H. by UiO. Part of the work at UiO was funded by Familien Blix fond (grant to H.J. and U.K.). The ALM Holding Company and the Mathy family provided benefactor support.

We thank Genentech for kindly providing us with purified MINT1526A antibody (proposal OR-217280). We thank the departments and core facilities that supported the generation and analysis of data. Electron microscopy data were generated using the Fred Hutchinson Cancer Center Electron Microscopy shared resource. The EMSR is supported in part by the Cancer Center Support Grant NIH P30 CA15704. We would like to thank Theo Humphreys, Dr. Anvesh Dasari, and Steve MacFarlane for their microscopy assistance and knowledge. We are thankful for the Mayo Clinic Proteomics Core for purification of the Fab components, which is a shared resource of the Mayo Clinic Cancer Center (NIH P30 CA15083). We thank the Fred Hutchinson Cancer Center's High Performance Computing service for their support in data analysis (1S10OD028685-01). We acknowledge MAX IV Laboratory for time on Beamline BioMax under Proposal 20190447. Research conducted at MAX IV, a Swedish national user facility, is supported by the Swedish Research council under contract 2018-07152, the Swedish Governmental Agency for Innovation Systems under contract 2018-04969, and Formas under contract 2019-02496. At UiO, work was performed at the UiO Structural Biology Core Facilities, which are part of the Norwegian Infrastructure NORCRYST, supported by the Norwegian Research Council (grant 245828). We are grateful to Dr. Thamiya Vasanthakumar, Rachel Werther, Jeremy Hollis, and Andres Fernandez for comments on the manuscript.

Declaration of Interests

JBH is a current employee and owns stock in Nykode Therapeutics ASA, a clinical-stage biopharmaceutical company with a focus on cancer immunotherapies. CMA is a current employee at Genentech. All other authors declare no potential conflicts of interest.

Methods

Spheroid Assays. Experiments were pursued through Reaction Biology under project PQ20385, with modifications of a previously published protocol [63]**.** 400 human umbilical vein endothelial cells (HUVEC) were pipetted in a hanging drop to allow overnight spheroid aggregation. 50 HUVEC spheroids were then seeded in 0.9 mL collagen gel and pipetted into a 24 well plate to allow polymerization. The inhibitors combined with 25 ng/mL of VEGF-A were added after 30 minutes by pipetting 100 µL of a 10-fold concentrated working solution on top of the polymerized gel. Plates were incubated at 37°C for 24 hours before being fixed with 4% paraformaldehyde PFA. Sprouting intensity of HUVEC spheroids were captured using an inverted microscope and the digital imaging software NIS-Elements BR 3.0 (Nikon). Cumulative sprout length per spheroid (CSL) was quantitated using Wimsprout image analysis software. The mean CSL of 10 randomly selected spheroids are defined as an individual data point. For IC_{50} determination, raw data were converted into percent HUVEC sprouting relative to sprouting control (25 ng/mL VEGF-A), which was set to 100% and basal control (no VEGF-A), which was set to 0%. IC_{50} values were determined using GraphPad Prism with constraint of bottom to 0 and no top constraint using a nonlinear regression curve fit with variable hill slope.

2D-tube formation assay. Endothelial tube formation assays experiments were pursued through Creative Bioarray project CBADY0508. HUVEC were seeded at 5×10^5 cells/well in 2 mL of complete culture medium in 6-well plates and cultured in a 37°C and 5% CO_2 incubator. Prior to experimentation, the culture medium was removed. Cells were subsequently treated with 2 mL of culture medium (negative control), 15 ng/mL VEGF (positive control), and BIIG2 or MINT1526A (1, 10, and 100 nM) supplemented with VEGF (15 ng/mL), then incubated at 37°C for 24 hours. Each condition was performed in triplicate. HUVECs were harvested and suspended in serum-free medium and then seeded in Matrigel-coated wells at the density of 1.5×10^5/1 mL/well. The cells were incubated at 37°C for 6 hours to allow tube formation. The total master segments length (pixels) and the number of meshes were counted using ImageJ software [64]. Three representative images were taken for each well at 40X magnification under an inverted microscope and the mean measurement was used as the individual data point. Statistical analysis was done using a T-test with a Bonferroni correction against the control group (HUVEC + VEGF).

Mouse models. Harlan Sprague Dawley female athymic nude mice that are recessive for the nu mutation in the *Foxn1* gene (Envigo) was used. This mouse strain exhibits a non-functional thymus and are unable to generate cytotoxic effector cells and do not elicit a graft-versus-host response. Mice selected for experimentation were 6 to 7 weeks old, weighing approximately 20 to 30 grams. Their housing conditions involved a 12-hour light/dark cycle with ad libitum access to food and water.

The mice were randomized into treatment groups and monitored daily. Tumor cells (M12 or M15) embedded in Matrigel were injected subcutaneously into the flank of the athymic mice. In efficacy studies, groups of mice (10 per group) with flank tumors were administered treatment once the tumor volumes

became palpable (approximately 50 to 100 mm^3). The flank tumors were measured three times a week. Treatment was administered twice weekly at a dose of 10 mg/kg. The experiments were concluded when the average tumor volume in the control group exceeded 1,000 mm^3. All experimental procedures adhered to the Principles of Laboratory Animal Care (NIH) and were approved by the Institutional Animal Care and Use Committee (Mayo Clinic). Statistical analysis was a T-test with Bonferroni correction against the control group (IgG). Experiments with Pentamidine were corrected against the control group (IgG).

Cell Culture and tissue samples

Hybridoma Cell Lines. All hybridomas were purchased from the Developmental Studies Hybridoma Bank. The BIIG2 hybridoma was deposited by Caroline Damsky [19]. The P1D6, P1F6, P3G8, and P5H9 hybridomas were deposited by Elizabeth Wayner and William Carter [65,66].

Patient-Derived Melanoma Cell Lines. Short-term cultures of human primary melanoma cells M12 and M15 were maintained through serial passages in immune-deficient mice via subcutaneous flank implantation, as previously described [67,68]. Dulbecco's modified Eagle's medium supplemented with 10% (v/v) fetal bovine serum (FBS) and antibiotics (penicillin, 100 U/mL, and streptomycin, 100 µg/mL) was used for growing the explant cultures. The cells were kept at 37°C in a humidified incubator with 5% CO_2.

Normal Human Melanocytes. Primary human neonatal epidermal melanocytes were obtained from Lifeline Cell Technology and subsequently cultured using DermaLife M Melanocyte Complete Medium, also provided by Lifeline Cell Technology.

Human tissue samples. A 23 core normal human formalin-fixed paraffin-embedded (FFPE) tissue microarray was purchased from Bio SB (BSB 0298). FFPE tissue of patient-derived nevi and melanoma were obtained through an institutional tissue registry. The Mayo Clinic Institutional Review Board approved the human investigations performed in this study following the Department of Health and Human Services requirements, where appropriate.

Immunohistochemistry. Proteins of interest were detected using the Leica Biosystems BOND-MAX autostainer platform in combination with primary antibody **(complete list in Supplemental Table S6)**, post-primary antibody, and a BOND Polymer Refine Red Detection system (DS9390; Leica Biosystems). Heat-induced antigen retrieval was by BOND EDTA-based pH 9.0 epitope retrieval solution 2 (AR9640; Leica Biosystems) applied for 20 minutes. All stains were digitized with a Leica Aperio ScanScope system.

Flow cytometry. Normal human melanocytes, M12 and M15 melanoma cells were stained using primary antibodies **(complete list in Supplemental Table S6)** against cell surface proteins as shown and

PE-labeled secondary antibodies. The BD Bioscience FACScaliber flow cytometer was utilized for data acquisition, and the acquired data was analyzed using FlowJo software.

Quantitative Microfluidic PCR. Our approach to PCR was as previously described [69]. RNA from cells was isolated using the RNeasy Plus Mini Kit (Qiagen). One microgram of total RNA was transcribed into cDNA using the SuperScript III Reverse Transcriptase (Thermo Fisher Scientific) and preamplified using TaqMan Preamp Master Mix (Thermo Fisher Scientific). Quantitative reverse transcriptase PCR was then performed using the Fluidigm BioMark HD system and dynamic array-integrated fluid circuits (Fluidigm). After thermal cycling, raw Ct (threshold cycles) data were checked for linear amplification. Gene expression was corrected by the mean of housekeeping genes (RLP0, RLP8, and β-actin) using the ΔCt method. Gene expression input for data analysis was ΔCt. The complete list of primers (HPLC purified, Integrated DNA Technologies) used for cDNA amplification by quantitative PCR are described in **Supplemental Table S7**.

Recombinant α5β1 plasmid design. The sequence of the α5 and β1 subunit wild-type ectodomain was incorporated into a CDNA3.1-Hygro(-)-TET template (Invitrogen). The integrin amino acid numbering starts after the signal peptide. Each integrin subunit was fused with either an ACID or a BASE coiled-coil peptide to assist in heterodimer production [70]. Residues 1 to 954 of the α5 subunit were cloned followed by a HRV-3C protease cleavage recognition site, an ACID coil, and a Strep-Tag II. The residues 1-728 of the β1 subunit were put into the same plasmid backbone filled by a HRV-3C protease cleavage recognition site, a BASE coil, and a 6x histidine tag.

Purification of integrin α5β1 ectodomain. Soluble integrin ectodomain (α5 residues 1-954 and β1 residues 1-728) was expressed using ExpiCHO cells (Thermo Fisher) in suspension at a density of 3.0×10^6 cells/mL by transient transfection using the ExpiCHO transfection kit. Cultures were co-transfected with plasmids encoding the α5 or β1 subunit in a 2:1 (α:β) ratio with Expifectamine CHO. Expression was according to the manufacturer's 'max titer' protocol. Phenylmethylsulfonyl fluoride (PMSF) was added to a final concentration of 0.5 mM. Clarified supernatant was diluted 1:1 v/v with Histrap binding buffer (20 mM Na_2PO_4, 500 mM NaCl, and 20 mM imidazole pH 7.4) and applied to 5 mL Histrap FF Crude column (Cytiva) equilibrated with Histrap binding buffer. The column was washed with 1 column volume (CV) of Histrap binding buffer before eluting protein with 2 CV of Histrap Elution Buffer (20 mM Na_2PO_4, 500 mM NaCl, and 500 mM imidazole pH 7.4). Protein fractions were pooled, concentrated and buffer exchanged into integrin storage buffer (20 mM Tris-Base pH 7.4, 150 mM NaCl, 1 mM $CaCl_2$, and 1 mM $MgCl_2$). Protease was added 1:20 w/w (protease:α5β1) to cleave the ACID/BASE coils and purification tags at 4°C overnight with rocking. The cleaved α5β1 integrin was further purified via gel filtration chromatography using a Superdex 200 Increase 10/300 SEC column (Cytiva) equilibrated in integrin storage buffer. Peak fractions of α5β1 were pooled, concentrated, flash frozen with 10% glycerol (v/v), and stored at -80°C until used for experiments.

Purification of BIIG2 and MINT1526A Fab fragments. BIIG2 antibody was produced at scale through the Mayo Clinic institutional core facility. Briefly, the production process involved culturing cells in roller bottles containing Iscove's Modified Dulbecco's Medium supplemented with gamma globulin-free serum. A single-step Protein G affinity purification was used to isolate antibodies. Antibodies were pooled, concentrated, and buffer exchanged into phosphate buffered saline (1x PBS). The concentrated stock solutions of the antibodies were stored at -80℃ until used for experiments. Genentech has kindly provided us with purified MINT1526A antibody.

BIIG2 and MINT1526A antibodies were digested with the Pierce Fab Preparation Kit (Thermo Fisher) using papain and following the manufacturer's protocol. BIIG2 Fab fragments were separated from the Fc fragments and intact IgG by loading onto a chromatography column packed with 5 ml of CaptureSelect IgG-Fc (Multi-species) Affinity Resin (Thermo Fisher) in PBS using a NGC FPLC instrument (Bio-Rad). The Fab fragment was present in the flow through. Separation of the MINT1526A Fab fragment from the Fc fragment was achieved using a NAb Protein A spin column following manufacturer's protocol. SDS-PAGE gel bands of Fab and Fc samples from both antibodies were digested and analyzed by mass spectrometry (Mayo Clinic Proteomics Core) to verify the identity and separation of the two fragments.

Crystallization of BIIG2. BIIG2 Fab was further purified using cation exchange chromatography (HisTrap SP HP, Cytiva) using a 0-100% gradient with CIEX elution buffer (25 mM Bis-Tris-HCl, 1 M NaCl at pH 6.5) and concentrated to 10 mg/mL in the CIEX elution buffer before crystallization. Crystallization conditions for BIIG2 Fab were screened with the sitting-drop vapor diffusion technique at 20°C, using commercial formulations (JCSG+, Morpheus, PACT Premier, Molecular Dimensions/CalibreScientific Inc.). The crystal used for data collection was obtained upon optimization of the initial hits, after equilibrating a 1:1 (v/v) mix of 300 nL CIEX-purified BIIG2 (7.6 mg/mL) with a crystallization solution consisting of 20% w/v PEG 3350, 0.2 M sodium chloride, 2.5% v/v DMSO. The crystal was cryo-protected with glycerol and flash-cooled before X-ray data collection. A complete detailed description of the CIEX purification protocol, crystal screening and optimization can be found in the **Supplemental Materials**.

X-ray data collection, crystal structure determination and refinement. Synchrotron data for BIIG2 Fab crystals were collected at the BioMAX beamline (MAX IV, Lund, Sweden). The highest-resolution data set, reported here, included data to 1.4 Å resolution. The structure was solved by molecular replacement using the Fab fragment of a rat monoclonal antibody (PDB ID: 1C5D) [71] as a search model, which had approximately 80% sequence identity with BIIG2. Software used for the analysis was primarily from *CCP4* and Phenix program suites [72,73]. Position numbering in the final model was adjusted to match the Kabat scheme [74]. Details regarding data processing and refinement as well as statistics can be found in **Supplemental Materials and Table S1**. Map and coordinate files are deposited in the Protein Data Bank (PDB), accessible with PDB ID: 8R38. Figures were generated using PyMOL (Schrödinger Inc.), assigning secondary structure elements as defined by the SST web server [75].

Biolayer Interferometry. All binding experiments were performed on an Octet Red96e (Sartorius). MINT1526A was immobilized on Protein A biosensors (Sartorius). These sensors were hydrated using inactive running buffer (20 mM Tris-Base pH 7.4, 150 mM NaCl, 0.1% BSA, and 0.02% Tween20 with 5mM $CaCl_2$) for 15 minutes before subsequently being incubated with fresh inactive running buffer. MINT1526A was diluted with inactive running buffer to 5 ug/mL and loaded for 300 seconds before a 120 second baseline equilibration in the inactive running buffer. Association with integrin α5β1 ectodomain was carried out with a two-fold dilution series from 50nM to 1.56nM in inactive running buffer for 300 seconds before dissociating for 300 seconds. Experiments were repeated with active running buffer (20 mM Tris-Base pH 7.4, 150 mM NaCl, 0.1% BSA, and 0.02% Tween20 with 1mM $MnCl_2$). MINT1526A binding experiments were performed in triplicate for both inactive and active conditions.

Binding assays with BIIG2 began with hydrating AR2G biosensors (Sartorius) in water for 15 minutes, followed by an additional 1 minute incubation. The AR2G biosensors were then activated using 20 mM EDC and 10 mM s-NHS for 300 seconds (following manufacturer's protocol). BIIG2 antibody was diluted with 10 mM sodium acetate pH 5.0 to 5 ug/mL and loaded until a threshold shift of 2nm was achieved. Loading was immediately quenched in 1M ethanolamine for 300 seconds. A baseline equilibration step was performed in inactive running buffer for 120 seconds. Association with integrin α5β1 ectodomain was performed at a two-fold dilution series from 50nM to 1.56nM in inactive running buffer for 450 seconds before dissociating for 450 seconds. Experiments were repeated with active running buffer and each buffer condition was repeated for an additional two times.

Competitive binding assays (**Supplemental Figure 4**) were carried out where α5β1 was bound to MINT1526A or BIIG2 Fabs or FN 7-10 fragment in a 1:2 molar ratio 20 minutes prior to assay running in either active or inactive buffer. MINT1526A or BIIG2 antibodies or FN 7-10 used as immobilized ligands were loaded onto their respective biosensors (Protein A for MINT1526A and AR2G for BIIG2 and FN 7-10) at 5ug/mL. Experimental conditions and association and dissociation step times follow as described above.

Negative-stain EM sample preparation, data acquisition and processing. The α5β1-Fab complexes were formed using an 1:2 ratio of α5β1 to antibody Fab, incubated at room temperature for 20 minutes, and diluted to a final concentration of 7.5 ug/mL in 20 mM Tris-base pH 7.4, 150 mM NaCl supplemented with either 5 mM $CaCl_2$ or 1 mM $MnCl_2$. For all experiments, 3 µL of protein sample was added to a glow-discharged (PELCO easiGlow; 30 seconds; 15 mA) carbon-coated copper grid (homemade carbon layer). The specimens were stained with 3 µL of 2% (wt/vol) uranyl formate solution as previously described [76].

Data were acquired using a Thermo Fisher Scientific Talos L120C transmission electron microscope operating at 120kV and recorded on a 4k x 4k Thermo Fisher Scientific Ceta camera at a nominal magnification of 92,000x with a pixel size of 1.58 Å/px. Leginon [77] was used to collect 252 (apo

α5β1 inactivating), 253 (apo α5β1 activating), 385 (α5β1:BIIG2 inactivating), 399 (α5β1:BIIG2 activating), 422 (α5β1:MINT1526A inactivating) and 482 (α5β1:MINT1526A activating) micrographs with a nominal range of 1.7-2.0 µm under focus and a dose of approximately 50 $e^-/Å^2$. The contrast transfer function of each micrograph was estimated using GCTF [78], and particles were automatically picked unbiasedly using Gautomatch ([78], htttp://www.mrc-lmb.cam.ac.uk/kzhang/Gautomatch). Particles were extracted at 352 pixels and binned to 128 pixels using RELION3 [79] before being imported into cryoSPARC [80]. Particles were subjected to multiple rounds of reference-free 2D alignment and classification to remove false positive particle images. The final particle count contributed to 2D class averages were 26,057 (apo α5β1, inactivating), 31,786 (apo α5β1, activating), 18,200 (α5β1:BIIG2, inactivating), 16,797 (α5β1:BIIG2, activating), 9,742 (α5β1:MINT1526A, inactivating) and 41,387 (α5β1:MINT1526A, activating).

Cryo-EM sample preparation. α5β1-BIIG2/MINT1526A Fab complexes were formed using a 1:2 α5β1 to Fab ratio in inactivating buffer (20 mM Tris pH 7.4, 150 mM NaCl, 5 mM $CaCl_2$) at room temperature with rocking for 20 minutes. Inactivating conditions were used to drive the equilibrium toward a more homogenous sample since we had already established that the epitope binding site was nowhere near the relevant cation coordination sites. These protein complexes were subjected to size exclusion chromatography using a Superdex200 Increase 10/300 GL (Cytiva) equilibrated with inactivating buffer. Fractions of α5β1:BIIG2/MINT1526A Fab were pooled and concentrated to 0.15 mg/mL before 3 uL of the protein sample was placed on a glow discharged (PELCO easiGlow; 30 seconds; 15 mA) R1.2/1.3 Au 300-mesh grid (QUANTIFOIL), blotted for 8 seconds with a blot-force of 1, and plunge-frozen immediately in liquid ethane using a Thermo Fisher Scientific Vitrobot Mark IV at 4° C and 100% humidity.

Cryo-EM Data collection and processing. Two datasets (one each for α5β1:BIIG2 Fab and α5β1:MINT1526A Fab) were acquired on a Thermo Fisher Scientific Glacios cryo-transmission electron microscope operating at 200kV and recorded with a Gatan K3 Direct Detection Camera. Automated data collected was carried out using the SerialEM software [81]. 99 frame movies were recorded in super-resolution mode with a super-resolution pixel size of 0.561 Å/px at a nominal magnification of 36,000x. Both datasets were collected in a single session with a nominal defocus range of 1.4–1.8 µm under focus and a dose of approximately 50$e^-/Å^2$. 3656 micrographs were collected of the α5β1:BIIG2 Fab complex and 3079 micrographs of α5β1:MINT1526A Fab.

The dose fractionated super-resolution image stacks were motion corrected and binned 2x2 by Fourier cropping using MotionCor2 [82]. Motion corrected images were then processed using CTFFIND4 within the cryoSPARC wrapper [80,83]. 2,425,530 (α5β1:BIIG2 Fab) and 1,101,393 (α5β1:MINT1526A Fab) particles were initially picked using the unbiased blob picker in cryoSPARC. These particles were subjected to multiple rounds of reference-free 2D alignment and classification in cryoSPARC. Next, particles were polished in Relion [84] and final 3D classification and refinement steps were done in cryoSPARC. The final particle count for α5β1:BIIG2 Fab is 371,066. The final particle count for

α5β1:MINT1526A Fab is 342,608. Images showing EM maps were generated using UCSF ChimeraX [85]. A detailed processing schematic is in **Supplemental Figure S9**.

CryoEM model building. The closed α5β1 headpiece (PDB: 3VI3) and our solved BIIG2 Fab structure were used as initial models for the α5β1:BIIG2 Fab complex. The half bent α5β1 ectodomain (PDB: 7NXD) was used as an initial model for α5β1:MINT1526A Fab complex. MINT1526A was modeled *de novo* using peptide sequences derived from mass spectrometry. Initial models were fitted into their respective cryoEM density using UCSF ChimeraX [85] and manually adjusted in COOT [86]. Glycosylations were manually added using COOT. Models (including glycans) were refined using Phenix and ISOLDE [87,88]. Modeling was aided by using sharpened and unsharpened cryoEM maps. BIIG2 and MINT1526A were numbered according to the Kabat numbering scheme [89]. CryoEM maps and model statistics are found in **Supplemental Table S2**.

Molecular dynamics simulations. All-atom molecular dynamics simulations were performed using the OpenMM 7.7.0 package [90] using AMBER ff19SB parameters and topologies. The initial structure for simulations were constructed from the α5β1:BIIG2 or α5β1:MINT152A cryoEM models. To reduce the system size, only the headpiece domains of α5β1 and variable domains of BIIG2 and MINT Fabs were simulated. N- and C- terminal residues were capped with acetyl and methyl amide groups, respectively. Protonation states for titratable residues were modeled based on a pH of 7.4. The systems were solvated in a truncated octahedron with the minimal distance between the solute and the box boundary set to 8Å and 150 mM NaCl. Calcium ions resolved in the cryoEM model were retained. The system was parameterized using the AMBER19ffSB [91] force field combined with the OPC water model and 12-6-4 Li Merz ion parameters [92]. As a control, an α5β1 without Fab bound, referred to as apo α5β1, was modeled and parameterized similarly.

The systems were first energy minimized for 20,000 steps followed by a gradual heating to 298K. During minimization and heating, protein backbone atoms were harmonically restrained by a 5 kcal/mol*$Å^2$ force constant. Production simulations were performed using periodic boundary conditions, hydrogen mass repartitioning [93], and a Langevin integrator with an integration timestep of 4 fs and collision rate of $\sqrt{2}$ ps^{-1}. Pressure was maintained at 1 atm using a MonteCarlo barostat with an update frequency of 100 steps. Nonbonded interactions were calculated with a distance cutoff of 10Å. Trajectory snapshots were saved every 100 ps during production simulations. A total of 7 replicates, 2μs each in length, were simulated for α5β1 systems.

Trajectories were processed using in-house scripts utilizing the CPPTRAJ [94], MDTraj 1.9.7 [95], and GetContacts (https://getcontacts.github.io/) packages. Hydrogen bond frequencies were calculated using a 3.5Å distance cutoff between the donor-hydrogen and acceptor atoms. The first 50 ns of production simulations were not included in analysis.

References

1. Hynes, R. O. Integrins: Bidirectional, Allosteric Signaling Machines. *Cell* **110**, 673–687 (2002).
2. Desgrosellier, J. S. & Cheresh, D. A. Integrins in cancer: Biological implications and therapeutic opportunities. *Nat. Rev. Cancer* **10**, 9–22 (2010).
3. Raab-Westphal, S., Marshall, J. F. & Goodman, S. L. Integrins as therapeutic targets: Successes and cancers. *Cancers* **9**, 1–28 (2017).
4. Slack, R. J., Macdonald, S. J. F., Roper, J. A., Jenkins, R. G. & Hatley, R. J. D. Emerging therapeutic opportunities for integrin inhibitors. *Nat. Rev. Drug Discov.* **21**, 60–78 (2022).
5. Avraamides, C. J., Garmy-Susini, B. & Varner, J. A. Integrins in angiogenesis and lymphangiogenesis. *Nat. Rev. Cancer* **8**, 604–617 (2008).
6. Arias-Mejias, S. M. *et al.* The role of integrins in melanoma: a review. *Int. J. Dermatol.* **59**, 525–534 (2020).
7. Hou, J., Yan, D., Liu, Y., Huang, P. & Cui, H. The roles of integrin α5B1 in human cancer. *Onco. Targets. Ther.* **13**, 13329–13344 (2020).
8. Takagi, J., Strokovich, K., Springer, T. A. & Walz, T. Structure of integrin α5β1 in complex with fibronectin. *EMBO J.* **22**, 4607–4615 (2003).
9. Schumacher, S. *et al.* Structural insights into integrin $\alpha_5\beta_1$ opening by fibronectin ligand. *Science Advances* **7**, eabe9716 (2021).
10. Kong, F., García, A. J., Mould, A. P., Humphries, M. J. & Zhu, C. Demonstration of catch bonds between an integrin and its ligand. *J. Cell Biol.* **185**, 1275–1284 (2009).
11. Friedland, J. C., Lee, M. H. & Boettiger, D. Mechanically activated integrin switch controls α5β 1 function. *Science* **323**, 642–644 (2009).
12. Leahy, D. J., Aukhil, I. & Erickson, H. P. 2.0 Å crystal structure of a four-domain segment of human fibronectin encompassing the RGD loop and synergy region. *Cell* **84**, 155–164 (1996).
13. Wierzbicka-Patynowski, I. & Schwarzbauer, J. E. The ins and outs of fibronectin matrix assembly. *J. Cell Sci.* **116**, 3269–3276 (2003).
14. Danen, E. H. *et al.* Emergence of alpha 5 beta 1 fibronectin- and alpha v beta 3 vitronectin-receptor expression in melanocytic tumour progression. *Histopathology* **24**, 249–256 (1994).

15. Kim, S., Bell, K., Mousa, S. A. & Varner, J. A. Regulation of angiogenesis in vivo by ligation of integrin alpha5beta1 with the central cell-binding domain of fibronectin. *Am. J. Pathol.* **156**, 1345–1362 (2000).
16. Bell-McGuinn, K. M. *et al.* A phase II, single-arm study of the anti-α5β1 integrin antibody volociximab as monotherapy in patients with platinum-resistant advanced epithelial ovarian or primary peritoneal cancer. *Gynecol. Oncol.* **121**, 273–279 (2011).
17. Kim, M.-Y. *et al.* Novel monoclonal antibody against beta 1 integrin enhances cisplatin efficacy in human lung adenocarcinoma cells. *J. Biomed. Res.* **30**, 217–224 (2016).
18. Weekes, C. D. *et al.* Phase I study of the anti-α5β1 monoclonal antibody MINT1526A with or without bevacizumab in patients with advanced solid tumors. *Cancer Chemother. Pharmacol.* **82**, 339–351 (2018).
19. Hall, D. E. *et al.* The alpha 1/beta 1 and alpha 6/beta 1 integrin heterodimers mediate cell attachment to distinct sites on laminin. *J. Cell Biol.* **110**, 2175–2184 (1990).
20. Damsky, C. H., Fitzgerald, M. L. & Fisher, S. J. Distribution patterns of extracellular matrix components and adhesion receptors are intricately modulated during first trimester cytotrophoblast differentiation along the invasive pathway, in vivo. *J. Clin. Invest.* **89**, 210–222 (1992).
21. Roskoski, R., Jr. Sunitinib: a VEGF and PDGF receptor protein kinase and angiogenesis inhibitor. *Biochem. Biophys. Res. Commun.* **356**, 323–328 (2007).
22. Schaffner, F., Ray, A. M. & Dontenwill, M. Integrin α5β1, the Fibronectin Receptor, as a Pertinent Therapeutic Target in Solid Tumors. *Cancers* **5**, 27–47 (2013).
23. Bhaskar, V. *et al.* A function blocking anti-mouse integrin alpha5beta1 antibody inhibits angiogenesis and impedes tumor growth in vivo. *J. Transl. Med.* **5**, 61 (2007).
24. Li, G. *et al.* Dual functional monoclonal antibody PF-04605412 targets integrin alpha5beta1 and elicits potent antibody-dependent cellular cytotoxicity. *Cancer Res.* **70**, 10243–10254 (2010).
25. Pietrobono, S. *et al.* ST3GAL1 is a target of the SOX2-GLI1 transcriptional complex and promotes melanoma metastasis through AXL. *Nat. Commun.* **11**, 5865 (2020).
26. Huang, R. & Rofstad, E. K. Integrins as therapeutic targets in the organ-specific metastasis of human malignant melanoma. *J. Exp. Clin. Cancer Res.* **37**, 92 (2018).

27. Lin, J. *et al.* Inhibiting S100B restores p53 levels in primary malignant melanoma cancer cells. *J. Biol. Chem.* **279**, 34071–34077 (2004).

28. Miyazaki, N., Iwasaki, K. & Takagi, J. A systematic survey of conformational states in β1 and β4 integrins using negative-stain electron microscopy. *J. Cell Sci.* **131**, (2018).

29. Mould, A. P., Barton, S. J., Askari, J. A., Craig, S. E. & Humphries, M. J. Role of ADMIDAS Cation-binding Site in Ligand Recognition by Integrin α5β1*. *J. Biol. Chem.* **278**, 51622–51629 (2003).

30. Nagae, M. *et al.* Crystal structure of α5β1 integrin ectodomain: Atomic details of the fibronectin receptor. *J. Cell Biol.* **197**, 131–140 (2012).

31. Campbell, M. G. *et al.* Cryo-EM Reveals Integrin-Mediated TGF-β Activation without Release from Latent TGF-β. *Cell* **180**, 490–501.e16 (2020).

32. Arimori, T. *et al.* Structural mechanism of laminin recognition by integrin. *Nat. Commun.* **12**, 4012 (2021).

33. Goldsmith, J. A., DiVenere, A. M., Maynard, J. A. & McLellan, J. S. Structural basis for non-canonical integrin engagement by Bordetella adenylate cyclase toxin. *Cell Rep.* **40**, 111196 (2022).

34. Adair, B. D., Xiong, J.-P., Yeager, M. & Arnaout, M. A. Cryo-EM structures of full-length integrin αIIbβ3 in native lipids. *Nat. Commun.* **14**, 4168 (2023).

35. Hollis, J. A., Chan, M. C., Malik, H. S. & Campbell, M. G. Evolutionary origin and structural ligand mimicry by the inserted domain of alpha-integrin proteins. *bioRxiv* 2023.11.05.565221 (2023) doi:10.1101/2023.11.05.565221.

36. Roy, A. *et al.* De novo design of highly selective miniprotein inhibitors of integrins αvβ6 and αvβ8. *Nat. Commun.* **14**, 1–18 (2023).

37. Valley, C. C. *et al.* The methionine-aromatic motif plays a unique role in stabilizing protein structure. *J. Biol. Chem.* **287**, 34979–34991 (2012).

38. Roman, J., Ritzenthaler, J. D., Roser-Page, S., Sun, X. & Han, S. alpha5beta1-integrin expression is essential for tumor progression in experimental lung cancer. *Am. J. Respir. Cell Mol. Biol.* **43**, 684–691 (2010).

39. Chiot, A. *et al.* Elevated α5 integrin expression on myeloid cells in motor areas in amyotrophic lateral

sclerosis is a therapeutic target. *Proc. Natl. Acad. Sci. U. S. A.* **120**, e2306731120 (2023).

40. Raghu, G. *et al.* A Phase IIb Randomized Clinical Study of an Anti-αvβ6 Monoclonal Antibody in Idiopathic Pulmonary Fibrosis. *Am. J. Respir. Crit. Care Med.* **206**, 1128–1139 (2022).
41. Cormier, A. *et al.* Cryo-EM structure of the αvβ8 integrin reveals a mechanism for stabilizing integrin extension. *Nat. Struct. Mol. Biol.* **25**, 698–704 (2018).
42. Xia, W. & Springer, T. A. Metal ion and ligand binding of integrin α5β1. *Proc. Natl. Acad. Sci. U. S. A.* **111**, 17863–17868 (2014).
43. Luo, B. H. & Springer, T. A. Integrin structures and conformational signaling. *Curr. Opin. Cell Biol.* **18**, 579–586 (2006).
44. Pang, X. *et al.* Targeting integrin pathways: mechanisms and advances in therapy. *Signal Transduct Target Ther* **8**, 1 (2023).
45. Ley, K., Rivera-Nieves, J., Sandborn, W. J. & Shattil, S. Integrin-based therapeutics: biological basis, clinical use and new drugs. *Nat. Rev. Drug Discov.* **15**, 173–183 (2016).
46. Ricart, A. D. *et al.* Volociximab, a chimeric monoclonal antibody that specifically binds alpha5beta1 integrin: a phase I, pharmacokinetic, and biological correlative study. *Clin. Cancer Res.* **14**, 7924–7929 (2008).
47. Figlin, R. A., Kondagunta, G. V., Yazji, S., Motzer, R. J. & Bukowski, R. M. Phase II study of volociximab (M200), an α5β1 anti-integrin antibody in refractory metastatic clear cell renal cell cancer (RCC). *J. Clin. Orthod.* **24**, 4535–4535 (2006).
48. Talavera, A. *et al.* Nimotuzumab, an antitumor antibody that targets the epidermal growth factor receptor, blocks ligand binding while permitting the active receptor conformation. *Cancer Res.* **69**, 5851–5859 (2009).
49. Lin, F.-Y. *et al.* A general chemical principle for creating closure-stabilizing integrin inhibitors. *Cell* **185**, 3533–3550.e27 (2022).
50. Wang, X. *et al.* De Novo design of integrin α5β1 modulating proteins to enhance biomaterial properties. *Adv. Mater.* e2500872 (2025).
51. Sundaram, A. *et al.* Targeting integrin α5β1 ameliorates severe airway hyperresponsiveness in experimental asthma. *J. Clin. Invest.* **127**, 365–374 (2017).

52. Budi, E. H. Pharmacological Inhibitors of Integrin αvβ6 That Differentially Modulate Protein Conformation Are Similarly Effective at Inhibiting Transforming Growth Factor Beta (TGF-β) Signaling in the Fibrotic Lung. (May 13-18 2022).
53. Praveen P. Tipirneni, Marc Schegerin, Robert E. Farrell Jr. *Annual Report, Form 10-K*. https://www.sec.gov/Archives/edgar/data/1679363/000167936322000010/morf-20211231.htm (2022).
54. Praveen P. Tipirneni, R. E. F., Jr. *Annual Report, Form 10-K*. https://www.sec.gov/Archives/edgar/data/1679363/000155837020001653/morf-20191231x10k.htm#FORM10KSUMMARY_744182 (2020).
55. Coulie, B. *Registration Statement, Form S-1*. https://www.sec.gov/Archives/edgar/data/1746473/000095012319004421/filename1.htm (2019).
56. John, A. E. *et al.* Translational pharmacology of an inhaled small molecule αvβ6 integrin inhibitor for idiopathic pulmonary fibrosis. *Nat. Commun.* **11**, 4659 (2020).
57. Cosgrove, G. P. PLN-74809, A Dual-Selective Inhibitor of αvβ6and αvβ1, Is Well Tolerated in Over 280 Healthy Participants. (May 13-18 2022).
58. Maden, C. H. *et al.* Safety, tolerability and pharmacokinetics of GSK3008348, a novel integrin αvβ6 inhibitor, in healthy participants. *Eur. J. Clin. Pharmacol.* **74**, 701–709 (2018).
59. Hersey, P. *et al.* A randomized phase 2 study of etaracizumab, a monoclonal antibody against integrin alpha(v)beta(3), + or - dacarbazine in patients with stage IV metastatic melanoma. *Cancer* **116**, 1526–1534 (2010).
60. National Library of Medicine, NCT00072930. *Clinicaltrials.gov* https://clinicaltrials.gov/study/NCT00072930.
61. Borst, A. J. *et al.* The Therapeutic Antibody LM609 Selectively Inhibits Ligand Binding to Human αVβ3 Integrin via Steric Hindrance. *Structure* **25**, 1732–1739.e5 (2017).
62. Hao, Y. *et al.* Synthetic integrin antibodies discovered by yeast display reveal αV subunit pairing preferences with β subunits. *bioRxiv* (2024) doi:10.1101/2024.01.26.577394.
63. Korff, T. & Augustin, H. G. Integration of endothelial cells in multicellular spheroids prevents apoptosis and induces differentiation. *J. Cell Biol.* **143**, 1341–1352 (1998).

64. Carpentier, G. *et al.* Angiogenesis Analyzer for ImageJ - A comparative morphometric analysis of 'Endothelial Tube Formation Assay' and 'Fibrin Bead Assay'. *Sci. Rep.* **10**, 11568 (2020).

65. Wayner, E. A., Orlando, R. A. & Cheresh, D. A. Integrins alpha v beta 3 and alpha v beta 5 contribute to cell attachment to vitronectin but differentially distribute on the cell surface. *J. Cell Biol.* **113**, 919–929 (1991).

66. Wayner, E. A., Carter, W. G., Piotrowicz, R. S. & Kunicki, T. J. The function of multiple extracellular matrix receptors in mediating cell adhesion to extracellular matrix: preparation of monoclonal antibodies to the fibronectin receptor that specifically inhibit cell adhesion to fibronectin and react with platelet glycoproteins Ic-IIa. *J. Cell Biol.* **107**, 1881–1891 (1988).

67. Carlson, B. L., Pokorny, J. L., Schroeder, M. A. & Sarkaria, J. N. Establishment, maintenance and in vitro and in vivo applications of primary human glioblastoma multiforme (GBM) xenograft models for translational biology studies and drug discovery. *Curr. Protoc. Pharmacol.* **Chapter 14**, Unit 14.16 (2011).

68. Gampa, G. *et al.* Brain Distribution and Active Efflux of Three panRAF Inhibitors: Considerations in the Treatment of Melanoma Brain Metastases. *J. Pharmacol. Exp. Ther.* **368**, 446–461 (2019).

69. Heim, J. B. *et al.* Myosin-1E interacts with FAK proline-rich region 1 to induce fibronectin-type matrix. *Proc. Natl. Acad. Sci. U. S. A.* **114**, 3933–3938 (2017).

70. Takagi, J., Erickson, H. P. & Springer, T. A. C-terminal opening mimics 'inside-out' activation of integrin α5β 1. *Nat. Struct. Biol.* **8**, 412–416 (2001).

71. Kontou, M. *et al.* The crystal structure of the Fab fragment of a rat monoclonal antibody against the main immunogenic region of the human muscle acetylcholine receptor. *Eur. J. Biochem.* **267**, 2389–2397 (2000).

72. Winn, M. D. *et al.* Overview of the CCP4 suite and current developments. *Acta Crystallogr. D Biol. Crystallogr.* **67**, 235–242 (2011).

73. Agirre, J. *et al.* The CCP4 suite: integrative software for macromolecular crystallography. *Acta Crystallogr D Struct Biol* **79**, 449–461 (2023).

74. Johnson, G. & Wu, T. T. Kabat Database and its applications: future directions. *Nucleic Acids Res.* **29**, 205–206 (2001).

75. Konagurthu, A. S., Lesk, A. M. & Allison, L. Minimum message length inference of secondary structure from protein coordinate data. *Bioinformatics* **28**, i97–105 (2012).

76. Ohi, M., Li, Y., Cheng, Y. & Walz, T. Negative Staining and Image Classification - Powerful Tools in Modern Electron Microscopy. *Biol. Proced. Online* **6**, 23–34 (2004).

77. Potter, C. S. *et al.* Leginon: a system for fully automated acquisition of 1000 electron micrographs a day. *Ultramicroscopy* **77**, 153–161 (1999).

78. Zhang, K. Gctf: Real-time CTF determination and correction. *J. Struct. Biol.* **193**, 1–12 (2016).

79. Zivanov, J. *et al.* New tools for automated high-resolution cryo-EM structure determination in RELION-3. *Elife* **7**, (2018).

80. Punjani, A., Rubinstein, J. L., Fleet, D. J. & Brubaker, M. A. CryoSPARC: Algorithms for rapid unsupervised cryo-EM structure determination. *Nat. Methods* **14**, 290–296 (2017).

81. Mastronarde, D. N. Automated electron microscope tomography using robust prediction of specimen movements. *J. Struct. Biol.* **152**, 36–51 (2005).

82. Zheng, S. Q. *et al.* MotionCor2: anisotropic correction of beam-induced motion for improved cryo-electron microscopy. *Nat. Methods* **14**, 331–332 (2017).

83. Rohou, A. & Grigorieff, N. CTFFIND4: Fast and accurate defocus estimation from electron micrographs. *J. Struct. Biol.* **192**, 216–221 (2015).

84. Zivanov, J., Nakane, T. & Scheres, S. H. W. A Bayesian approach to beam-induced motion correction in cryo-EM single-particle analysis. *IUCrJ* **6**, 5–17 (2019).

85. Pettersen, E. F. *et al.* UCSF ChimeraX: Structure visualization for researchers, educators, and developers. *Protein Sci.* **30**, 70–82 (2021).

86. Emsley, P., Lohkamp, B., Scott, W. G. & Cowtan, K. Features and development of Coot. *Acta Crystallogr. D Biol. Crystallogr.* **66**, 486–501 (2010).

87. Afonine, P. V. *et al.* Real-space refinement in PHENIX for cryo-EM and crystallography. *Acta Crystallogr D Struct Biol* **74**, 531–544 (2018).

88. Croll, T. I. ISOLDE: a physically realistic environment for model building into low-resolution electron-density maps. *Acta Crystallographica Section D: Structural Biology* **74**, 519–530 (2018).

89. Wu, T. T. & Kabat, E. A. An analysis of the sequences of the variable regions of Bence Jones

proteins and myeloma light chains and their implications for antibody complementarity. *J. Exp. Med.* **132**, 211–250 (1970).

90. Eastman, P. *et al.* OpenMM 7: Rapid development of high performance algorithms for molecular dynamics. *PLoS Comput. Biol.* **13**, e1005659 (2017).
91. Tian, C. *et al.* ff19SB: Amino-Acid-Specific Protein Backbone Parameters Trained against Quantum Mechanics Energy Surfaces in Solution. *J. Chem. Theory Comput.* **16**, 528–552 (2020).
92. Li, Z., Song, L. F., Li, P. & Merz, K. M., Jr. Systematic Parametrization of Divalent Metal Ions for the OPC3, OPC, TIP3P-FB, and TIP4P-FB Water Models. *J. Chem. Theory Comput.* **16**, 4429–4442 (2020).
93. Hopkins, C. W., Le Grand, S., Walker, R. C. & Roitberg, A. E. Long-Time-Step Molecular Dynamics through Hydrogen Mass Repartitioning. *J. Chem. Theory Comput.* **11**, 1864–1874 (2015).
94. Roe, D. R. & Cheatham, T. E., Iii. PTRAJ and CPPTRAJ: Software for Processing and Analysis of Molecular Dynamics Trajectory Data. *J. Chem. Theory Comput.* **9**, 3084–3095 (2013).
95. McGibbon, R. T. *et al.* MDTraj: A Modern Open Library for the Analysis of Molecular Dynamics Trajectories. *Biophys. J.* **109**, 1528–1532 (2015).

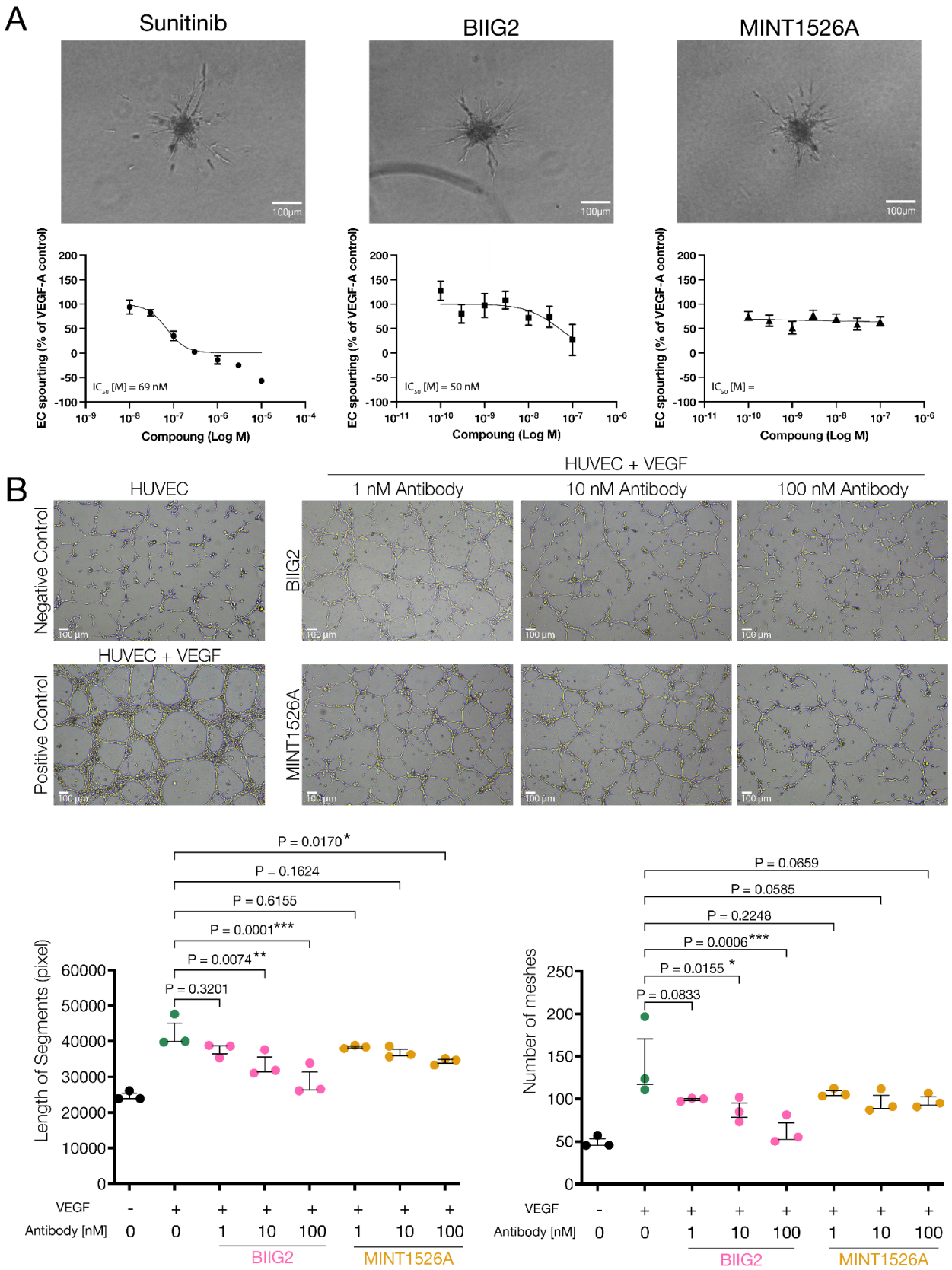
A
Sunitinib
BIIG2
MINT1526A
100µm
EC spourting (% of VEGF-A control)
Compoung (Log M)
IC50 [M] = 69 nM
IC50 [M] = 50 nM
IC50 [M] =
B
HUVEC
HUVEC + VEGF
1 nM Antibody
10 nM Antibody
100 nM Antibody
Negative Control
Positive Control
BIIG2
MINT1526A
100 µm
P = 0.0170*
P = 0.1624
P = 0.6155
P = 0.0001***
P = 0.0074**
P = 0.3201
Length of Segments (pixel)
P = 0.0659
P = 0.0585
P = 0.2248
P = 0.0006***
P = 0.0155 *
P = 0.0833
Number of meshes
VEGF
Antibody [nM]
BIIG2
MINT1526A

Figure 1. Effects of BIIG2 and MINT1526A α5 integrin antibodies on angiogenesis *in vitro*. (A) HUVEC spheroids were imaged and measured for cumulative sprout length (CSL). Scale bar is 100μm. Total sprouting measured was converted to sprouting relative to control (+VEGF), which was set to 100% and basal control (-VEGF) as 0%. IC_{50} graphs were generated using this relative data using a nonlinear regression curve fit with variable hill slope. Data shown are mean ± SEM; n = 10 spheroids per concentration. **(B)** Images of HUVEC tube formation on Matrigel after 24 hours of incubation in the presence or absence of antibodies. Scale bar is 100μm. HUVEC cultured in medium alone served as the basal control, whereas HUVEC treated with VEGF were used as the positive control. The quantification of tube formation involved measuring the total length of master segments (the cumulative length of tubes formed, measured in pixels) and the number of meshes using angiogenesis analyzer for imageJ [64]. Master segments and mesh counts were averaged from three fields of views per replicate, n=3 (9 total images). Data are shown as the mean ± SEM; n = 3; T-test with Bonferroni correction; adjusted P values are shown.

A

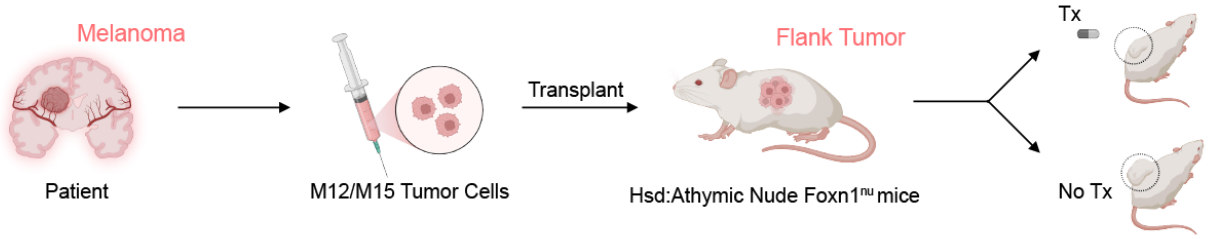
Melanoma
Patient
M12/M15 Tumor Cells
Transplant
Flank Tumor
Hsd:Athymic Nude Foxn1nu mice
Tx
No Tx

B

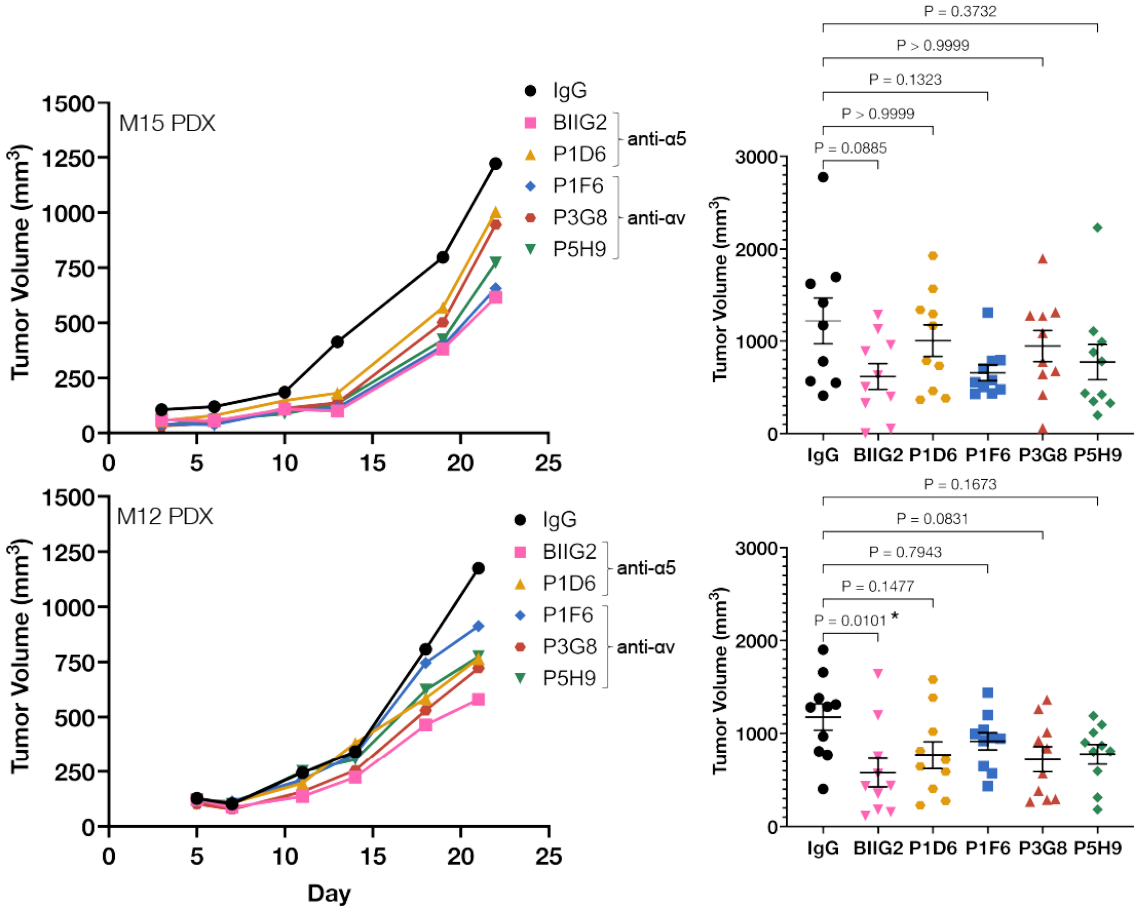
M15 PDX
M12 PDX
Tumor Volume (mm3)
Day
IgG
BIIG2
P1D6
P1F6
P3G8
P5H9
anti-α5
anti-αv
P = 0.3732
P > 0.9999
P = 0.1323
P > 0.9999
P = 0.0885
P = 0.1673
P = 0.0831
P = 0.7943
P = 0.1477
P = 0.0101*

C

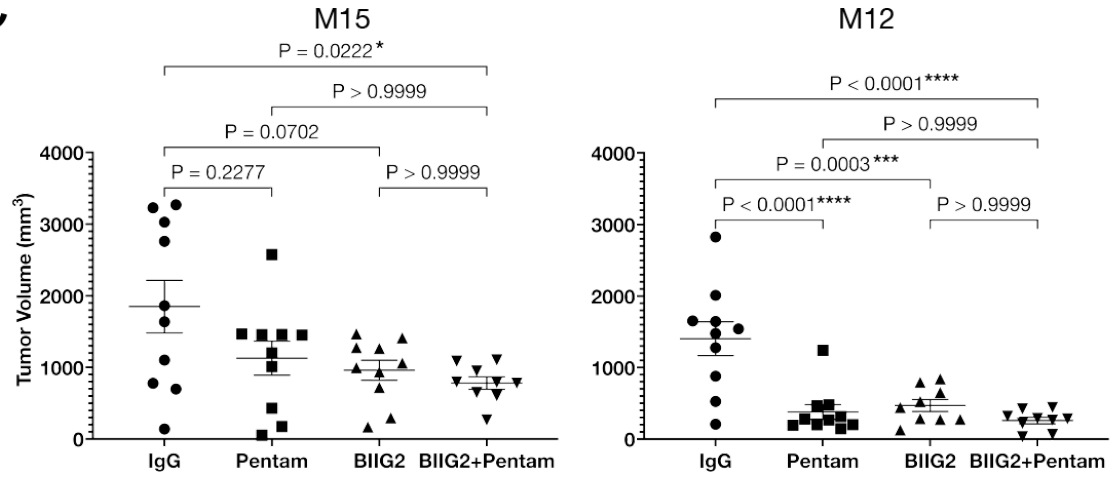
M15
M12
Tumor Volume (mm3)
P = 0.0222*
P > 0.9999
P = 0.0702
P = 0.2277
P > 0.9999
P < 0.0001****
P > 0.9999
P = 0.0003***
P < 0.0001****
P > 0.9999
IgG
Pentam
BIIG2
BIIG2+Pentam

Figure 2. *In vivo* anti-tumor activity of BIIG2. (A) Athymic nude mice were xenografted with patient-derived melanoma cells (labeled M15 and M12) from brain metastasis. Upon observation of palpable tumors, we proceeded with the treatment of the mice. Illustration created with BioRender.com. **(B)** Mice were injected intraperitoneally with BIIG2 or other αv and α5 integrin antibodies. Treatment was administered twice weekly at a dose of 10 mg/kg. Data plotted are shown from the final day of observation as mean + SEM; n = 10, except for M15 where IgG control n=9; T-test with Bonferroni correction; adjusted P values are shown. **(C)** For comparison, mice were treated orally with focal adhesion kinase inhibitors PF56-2271 and PND-1186 at doses of 25 mg/kg twice daily and 50 mg/kg twice daily, respectively. Pentamidine isethionate, an aromatic diamidine with anti-cancer activity, was administered intraperitoneally at a dose of 10 mg/kg once daily. Data shown are mean+ SEM; n = 10 mice per treatment group; T-test with Bonferroni correction; adjusted P values are shown.

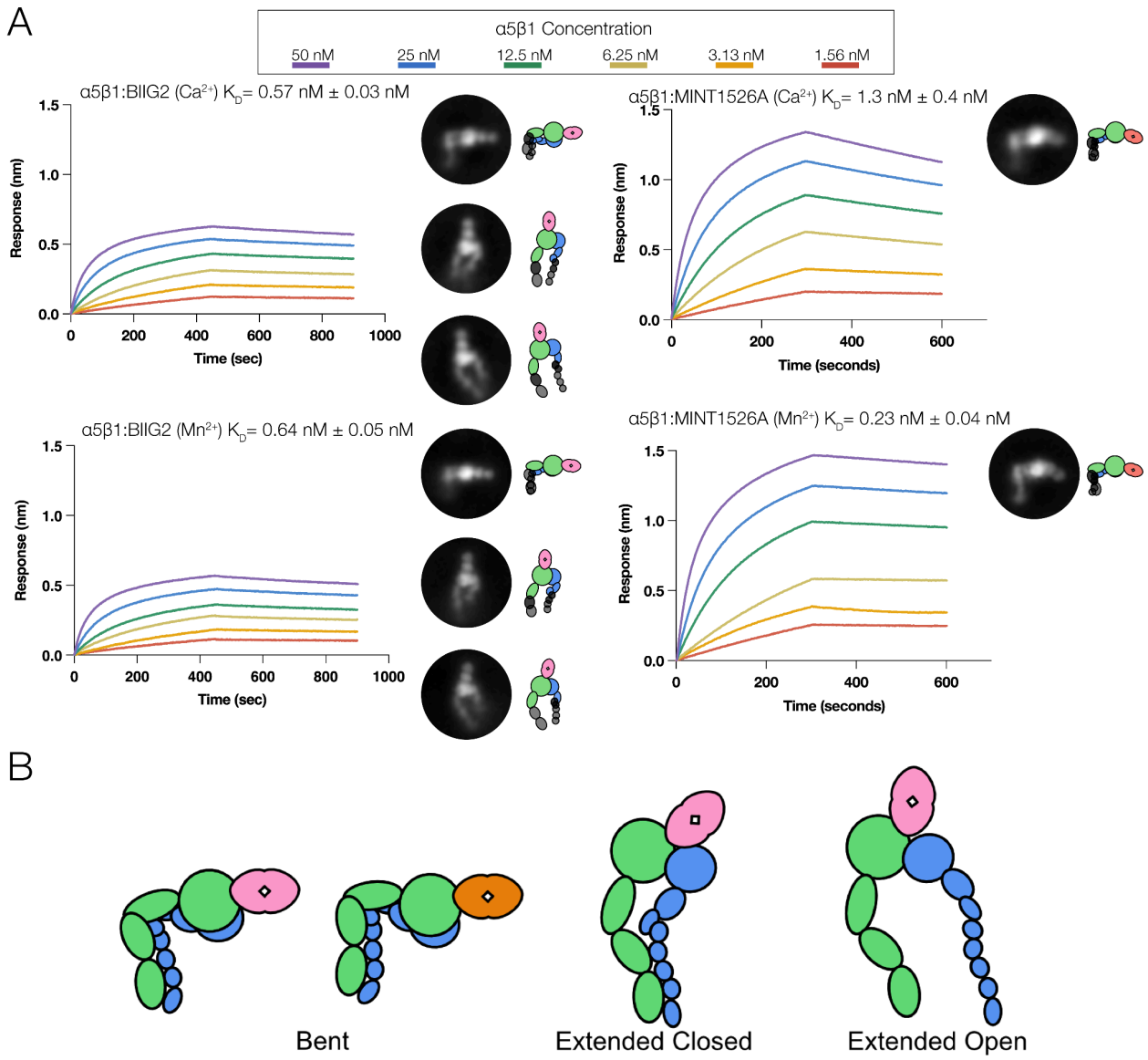

Figure 3. Biolayer interferometry binding kinetic analysis and negative stain electron microscopy of integrin-Fab complexes. (A) Representative BLI sensorgrams displaying the association and dissociation step of the binding assay between immobilized BIIG2 and MINT1526A and α5β1 integrin ectodomain in the presence of Ca^{2+} (inactivating) and Mn^{2+} (activating). BIIG2 binds to α5β1 ectodomain with an K_D of 0.57 nM and 0.64 nM in inactivating conditions and activating conditions respectively. MINT1526A binds to α5β1 ectodomain with an K_D of 1.3 nM and 0.23 nM in inactivating conditions and activating conditions, respectively. Each experimental condition was repeated three times with the affinities reported as the mean ± SEM. Representative negative stain EM 2D class averages of the α5β1 integrin in complex with the antibody Fab fragment in their respective buffer conditions. The complete set

of 2D class averages are in **Supplemental Figure 5**. **(B)** A cartoon schematic representing the conformations of integrin observed under negative stain EM with either BIIG2 or MINT1526A Fab bound. Pink, BIIG2; Orange, MINT1526A. Binding of BIIG2 Fab does not influence the conformational landscape of α5β1. MINT1526A bound-α5β1 is only observed in the half-bent conformation. The complete set of 2D class averages are in **Supplemental Figure 4**.

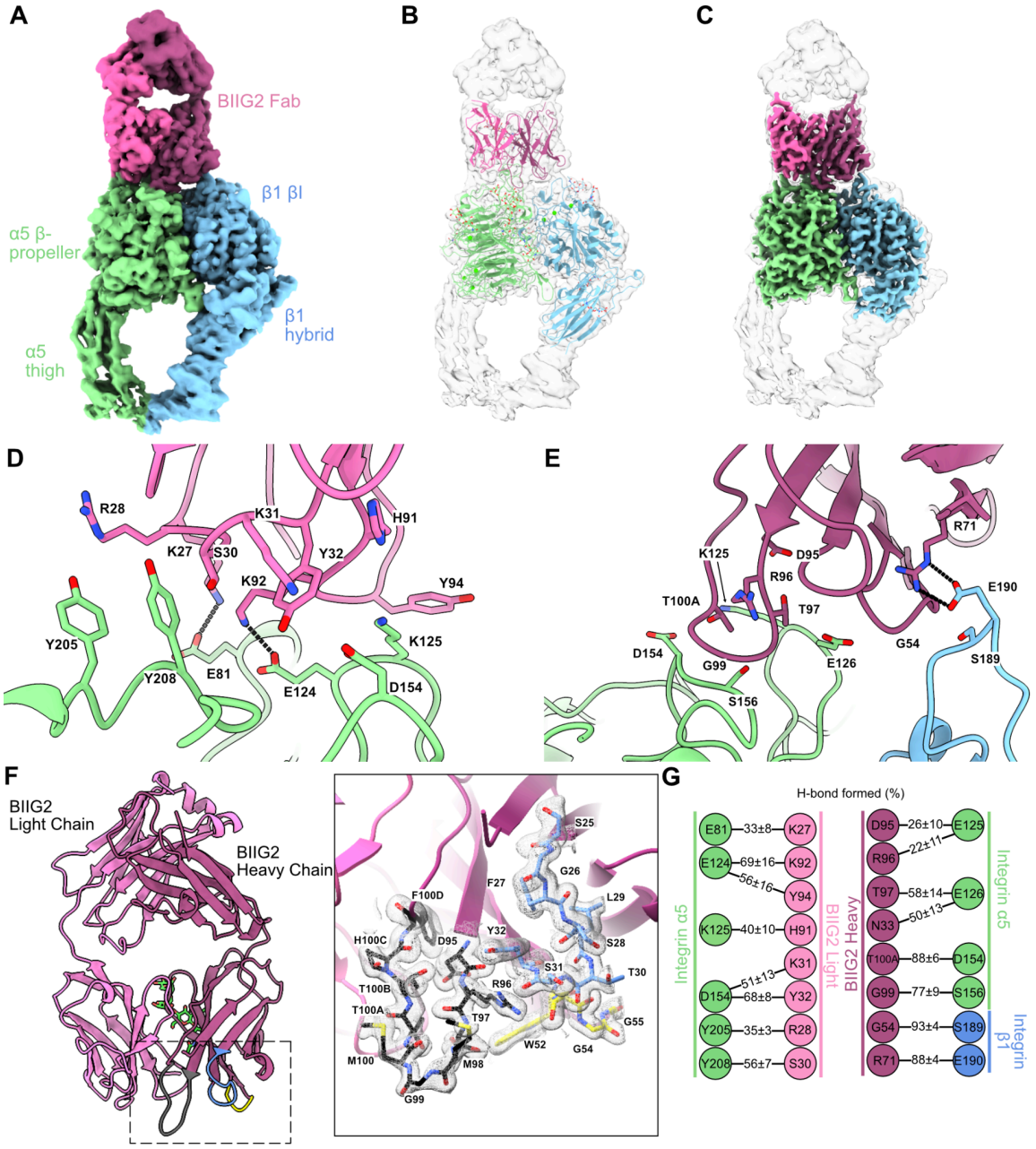

Figure 4. CryoEM analysis of integrin α5β1:BIIG2 Fab complex. (A) CryoEM density map of α5β1 ectodomain with BIIG2 Fab bound. The map is displayed as unsharpened and at a low threshold. The color code is as follows: integrin α5 subunit is green, integrin β1 subunit is blue, BIIG2 Fab light chain is light pink and heavy chain is dark pink. **(B)** Ribbon diagram of α5β1:BIIG2 Fab displayed within the density map shown in (A). **(C)** The sharpened cryoEM map is shown in color, superimposed with the unsharpened map in semi-transparent white. **(D and E)** A ribbon diagram shows a close-up view of the interface between α5β1 and the light chain **(D)** and heavy chain **(E)** of the BIIG2 Fab. Salt bridges are

drawn with dashed lines. **(F)** Crystal structure of BIIG2 Fab is shown in cartoon representation (light chain in light pink, heavy chain in dark pink). The single N-linked glycan N60 is shown as green stick representation. A close-up view of the Fab crystal structure shown in cartoon representation (dashed box), with σ_A-weighted $2F_o$-F_c electron density map (grey mesh, contoured at 1.0 σ) for selected residues of the CDR loops (CDR1-yellow, CDR2-blue, and CDR3-red), which are depicted in stick representation; amino acid residues are labeled. **(G)** Percentage of hydrogen bonds and salt bridges formed (mean ± SEM) between integrin α5β1 and BIIG2 Fab molecular dynamics simulations using a 3.5 Å cutoff between acceptor and donor-H atoms. Values were averaged across seven simulation repeats, each 2.0 μs long. Stable interactions are summarized in **Table S4.**

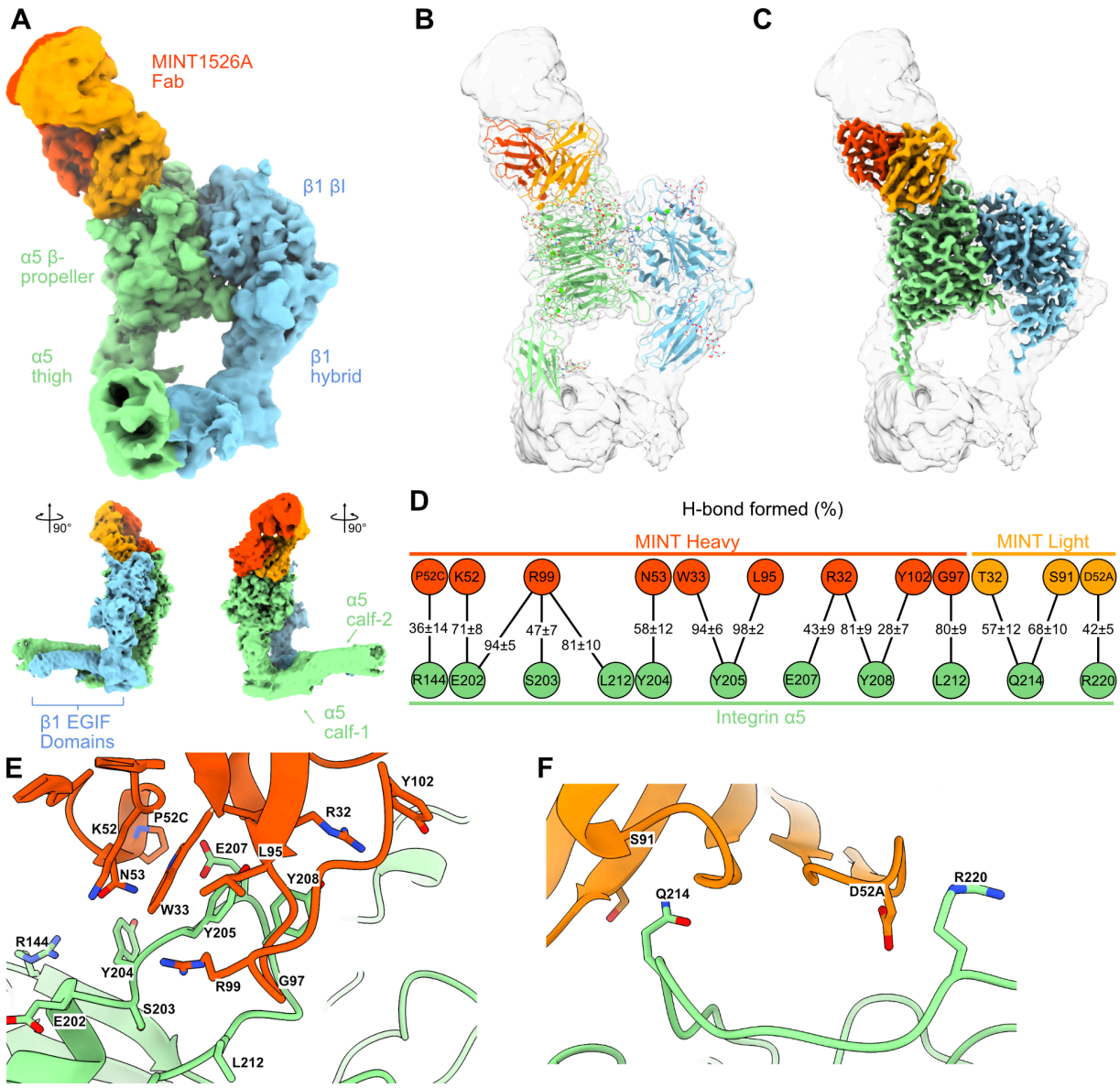

Figure 5. CryoEM analysis of α5β1:MINT1526A Fab complex. (A) CryoEM density map of α5β1 ectodomain with MINT1526A Fab bound. The map is displayed as unsharpened and at a low threshold. The color code is as follows: integrin α5 subunit is green, integrin β1 subunit is blue, MINT1526A Fab light chain is light orange and heavy chain is dark orange. **(B)** Ribbon diagram of α5β1:MINT1526A Fab displayed within the density map shown in (A). **(C)** The sharpened cryoEM map is shown in color, superimposed with the unsharpened map in semi-transparent white. **(D)** Hydrogen bonds identified between integrin α5β1 MINT1526A Fab are supported by molecular dynamics simulations. Percentage of hydrogen bonds formed (mean ± SEM) between integrin α5β1 and MINT1526A Fab using a 3.5 Å cutoff between acceptor and donor-H atoms. Values were averaged across seven simulation repeats, each 2.0

μs long. A ribbon diagram shows a close-up view of the interface between α5β1 and the MINT1526A Fab heavy chain **(E)** and light chain **(F)**. Stable interactions are summarized in **Table S5.**